metals

Article

An Analysis of the Mapping Relationship between Microstructure and Solidification Parameters during Aluminum Fused Coating

Guangxi Zhao *, Jialei Zhang and Xianhai Yang

School of Mechanical Engineering, Shandong University of Technology, Zibo 255000, China; three_stones0202@163.com (J.Z.)
* Correspondence: zgx2019@sdut.edu.cn

Abstract: Metal fused-coating technology has the advantages of both low cost and high efficiency and is a new additive manufacturing technology in recent years. The previous studies were mainly aimed at the optimization of process parameters and the control of the surface quality of parts, while there were few theoretical analyses on the microstructure morphology after solidification. A three-dimensional transient numerical model was established to calculate temperature gradient and solidification rate, considering the changes in material physical properties with temperature during the calculation process. The temperature gradient on the substrate surface is jointly affected by the melt flowing out of the nozzle and the welding arc. It was found that the solidification front of the aluminum alloy was in an unstable state during the coating process. When the value of G/R decreases, the microstructure of the solidification interface gradually changes from columnar crystals to columnar dendrites and equiaxial crystals. The microstructure at the bottom of both the molten pool and coating layer is columnar crystal, while the microstructure at the upper part is equiaxed crystal.

Keywords: metal fused coating; additive manufacturing; microstructure; 2024 aluminum

check for updates

Citation: Zhao, G.; Zhang, J.; Yang, X. An Analysis of the Mapping Relationship between Microstructure and Solidification Parameters during Aluminum Fused Coating. *Metals* **2023**, *13*, 1594. https://doi.org/10.3390/met13091594

Academic Editors: Antonio Riveiro and Antonello Astarita

Received: 31 July 2023
Revised: 12 September 2023
Accepted: 13 September 2023
Published: 14 September 2023

1. Introduction

Due to the advantages of high specific strength, low density, and good plasticity, 2024 aluminum alloy is widely used in the aerospace industry to produce various high-load parts and components, such as frame parts and skins on airplanes [1]. With the increasing demand for the integration of complex parts in various military and industrial fields, traditional machining methods have become increasingly inadequate. Metal additive manufacturing technology can realize the direct forming of complex 3D digital models into metal parts, which can effectively make up for the shortcomings of traditional processing technology [2,3]. Mainstream additive manufacturing technology usually uses high-power lasers [4], electron beams [5], or welding arcs [6] as heat sources and adopts powder or wire as raw materials. In recent years, a lot of effort has been put into improving the quality of additive manufacturing parts. For example, Gu [7] and Wang [8] studied the effect of particle reinforcement on laser additive manufacturing and found that the addition of a reinforcement phase significantly improved part performance. FU [9] uses hot wire for arc additive forming, effectively controlling pore defects. Nowadays, high-precision additive manufacturing technology can even process surface nanostructure and is widely used in military and medical fields [10–12]. However, since the equipment and materials are expensive and the production efficiency is relatively low [13], the application in the industrial production field is limited. Therefore, it is necessary to develop an efficient and low-cost aluminum alloy additive manufacturing technology.

Microstructure morphology plays an important role in the mechanical properties of metal components [14]. The research on the microstructure evolution process has great significance in obtaining the desirable microstructure and controlling the performance of parts [15]. In melting-based additive manufacturing, once the material is irradiated by a high-energy beam, the local temperature will instantly surge above the melting point and form a micro-molten pool. The cooling rate of additive manufacturing can reach 10^2~10^6 K/s, which is much higher than casting [16]. As a result, the mechanisms of the microstructure evolution are different, too. The main methods for microstructure simulation include the phase field method [17], cellular automation [18], and the Monte Carlo method [19]. Hosseinzadeh simulated the microstructural evolution of NiTi alloys through a multiscale numerical model, which is divided into two parts: thermal analysis and microstructure evolution [20]. Panchenko assessed the microstructure transformations using the calculated continuous cooling transformation (CCT) diagram [21]. Yan established a microstructure evolution model based on finite difference–cellular automaton and found that dendrites were refined with increasing cooling rates [22]. Xue proposed a physics-embedded graph network and improved computing speed by 50 times compared to traditional direct numerical simulation [23]. Due to complex thermal conditions, the quantitative relationship between process parameters and solidification factors is still missing.

The metal fused-coating process was originally proposed by our research group as a novel additive manufacturing technology [24]. The schematic diagram of the metal fused-coating equipment is shown in Figure 1. Electromagnetic induction heating is used in combination with a graphite crucible to melt the raw materials, such as bars and blocks. Aluminum alloy melt is less prone to bonding with the graphite at high temperatures, so the crucible made of graphite material is more conducive to cleaning and can effectively reduce the resistance of melt flowing from the nozzle. The melt temperature in the crucible is precisely controlled by a temperature controller, and the melt flows out of the nozzle under pressure above the liquid level. In order to prevent the aluminum alloy melt from blocking the nozzle after oxidation and avoid oxide inclusion inside the forming part, the whole forming process is carried out in an argon glove box. The nozzle remains stationary while the substrate mounted on the translation platform moves in three dimensions during the coating process.

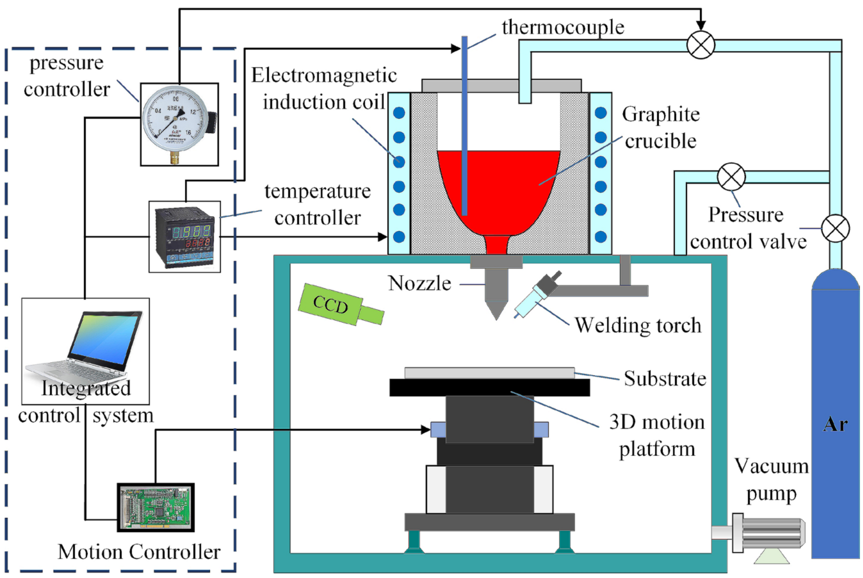

Figure 1. The schematic diagram of the metal fused-coating equipment.

A schematic diagram of the local forming area of the fused coating is shown in Figure 2. The molten aluminum alloy flows out of the nozzle and then spreads around under the squeeze of the nozzle until it is completely solidified. The 3D motion platform moves according to the layered trajectory of the processed parts. After the current layer has been deposited, the 3D motion platform descends by one layer and begins processing the next layer. In order to achieve metallurgical bonding between adjacent deposition layers to improve interlayer bonding strength, the AC pulse TIG arc is used for preheating.

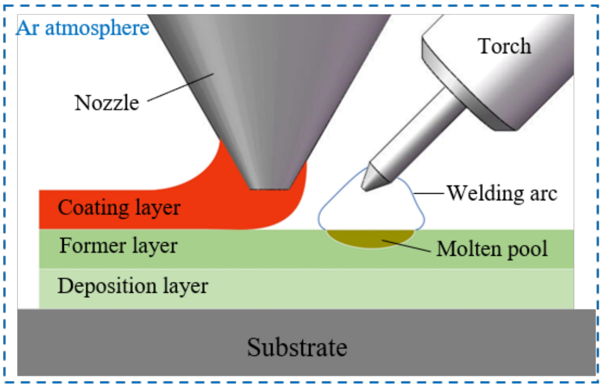

Figure 2. Schematic diagram of the local forming area.

The previous research on fused coating mainly focused on the control of forming quality, the influence of process parameters, and numerical analysis of the heat flow field. Fang studied the influence of process parameters on the width and height of the deposition layer to improve the surface quality of the formed parts [25]. Wang [26] designed a laser band-pass composite filter sensing system to realize dynamic control of deposition layer dimension during fused coating. Zhao [27] studied the driving forces of the preheating arc during the fused-coating forming process and predicted the cross-sectional morphology of the deposition layer. Du developed a 3D-thermal FVM model to calculate the temperature field and macromorphology of parts [28]. However, there was relatively little theoretical analysis of microstructure morphology during fused coating. This paper intends to reveal the mapping relationship between microstructure character and solidification parameters based on classical solidification theory [29].

2. Materials and Methods

The numerical analysis model and boundary conditions are shown in Figure 3. Flow-3D is based on the finite-difference method and meshes the entire computing domain rather than individual components. For a clearer representation of the model, the spatial mesh is hidden. The upper boundary is set as the pressure boundary, and a fluid source phase is set at the upper boundary, which can continuously provide high-temperature aluminum alloy melt for the coating nozzle. The model adopts relative pressure, so the atmospheric pressure was set to zero. Due to the symmetry of the model, the XOZ plane is set as the symmetric boundary. The bottom boundary is set as a wall, and the remaining boundaries are set as continuous boundaries. The pulse frequency of the welding machine current is 5 Hz, and the base current and peak current are 120 A and 200 A, respectively. The nozzle temperature is constant at 973 K, while the initial temperature of the substrate and the ambient is 298 K.

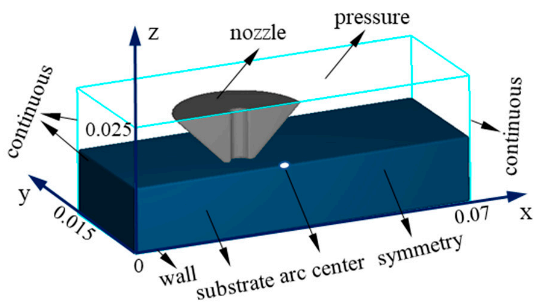

Figure 3. Numerical analysis model and boundary conditions.

The generalized minimum residual solver (GMRES) was chosen for pressure calculation due to its rapid convergence and parallel efficiency. The multiplier for the dynamically adjusted convergence criterion is set to 0.85, while the explicit solvers were adopted for the calculation of heat transfer and viscous stress, and the maximum number of iterations is set to 8000. In the calculation of this article, the residual and heat balance standards are set to $R \leq 10^{-4}$, $0.999 \leq \theta \leq 1.001$. It was found through calculation that the impact of higher convergence standards on the results can be ignored.

High-purity 2024 aluminum alloy bars are used as raw materials, and the surface oxide skin is polished off with sandpaper before being placed in a crucible. The chemical composition and its mass fraction of 2024 aluminum alloy are shown in Figure 4.

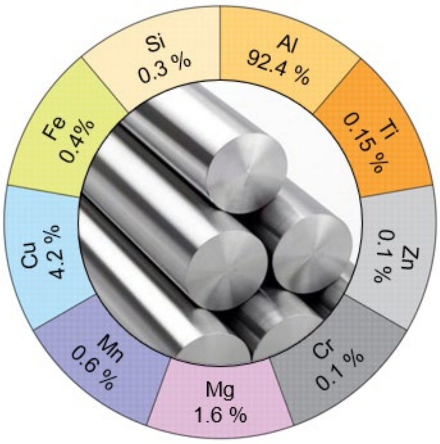

Figure 4. The chemical composition and its mass fraction of 2024 aluminum alloy.

The thermal physical property parameters of 2024 aluminum alloy were calculated by JMatPro, and the changes of specific heat, heat transfer coefficient, density, and viscosity with temperature were also considered during numerical calculation. The arc driving forces, such as surface tension, buoyancy, arc pressure, Lorentz force, and drag force, were all added to the model through self-programming.

In the rapid solidification process of metals, undercooling is a key parameter for controlling dendrite growth [30]. The boundary of the solid−liquid interface was determined by numerical calculation results, and the average temperature gradient and solidification rate were used to speculate on the internal microstructure of the aluminum alloy after solidification. Figure 5 is a schematic diagram for calculating the average temperature gradient in the molten pool.

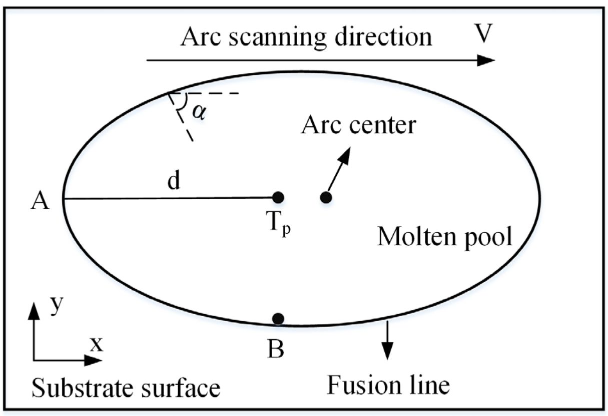

Figure 5. Schematic diagram for calculating the average temperature gradient.

As shown in Figure 5, point A is the intersection of the fusion line and the centerline of the melt pool, and T_p is the peak temperature inside the molten pool. The average temperature gradient along the specified plane in the molten pool is defined as [31]:

$$\mathrm{G} = \frac{T_p - T_s}{d} \tag{1}$$

where G is the average temperature gradient, T_s is the solid phase temperature, and d represents the distance between point A and the peak temperature point.

During the arc preheating process, the movement direction of the solidification front of the molten pool always follows the maximum thermal gradient direction perpendicular to the solid−liquid interface. The temperature gradient varies at various points on the fusion line and the solidification rate at the solid−liquid interface in the stable section can be defined as [31]:

$$\mathrm{R} = \mathrm{V} \cdot \cos\alpha \tag{2}$$

where R is the solidification rate in the stable section of the molten pool, V is the arc scanning velocity, and α is the angle between the normal direction of the solid−liquid fusion line and the scanning direction.

As shown in Figure 6, d_H and d_V are the distances from the molten pool center along the horizontal plane and the vertical plane to the boundary, respectively. Then, the solidification velocity in the horizontal and vertical directions can be expressed as:

$$\mathrm{R}_H = \frac{d}{dt}(d_{\mathrm{H}}) \tag{3}$$

$$\mathrm{R}_V = \frac{d}{dt}(d_{\mathrm{V}}) \tag{4}$$

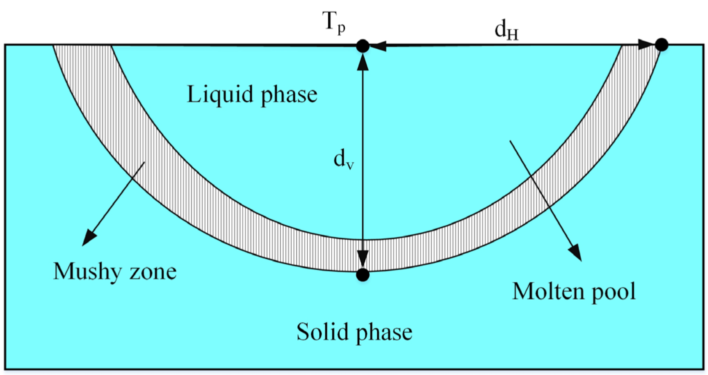

Figure 6. Diagram of average temperature gradient of molten pool cross section.

3. Results

The ratio of average temperature gradient to solidification rate (G/R) and its product (G·R) are important factors affecting the microstructure morphology and scale of molten pool solidification. When the value of G/R increases, the microstructure morphology at the interface transitions from equiaxed dendrites to cellular dendrites. The isotherms of the substrate surface at different times are shown in Figure 7.

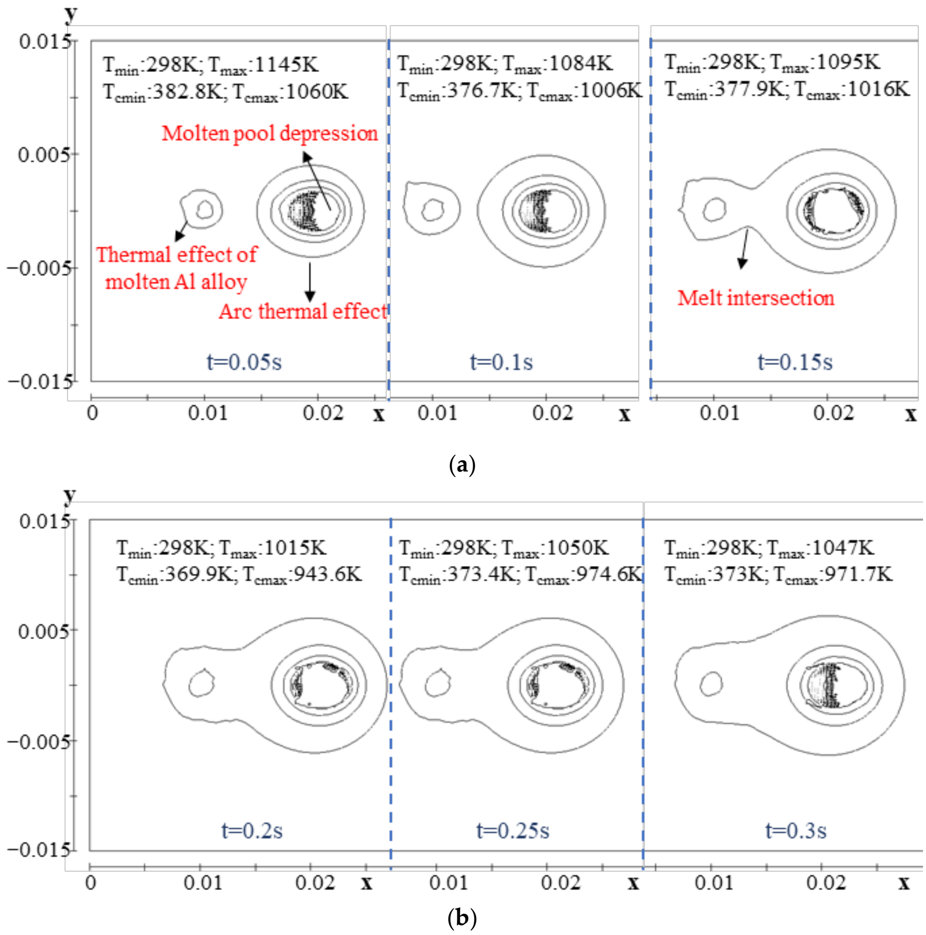

Figure 7. The isotherms of the substrate surface at different times. (**a**) Time at 0.05 s, 0.1 s, and 0.15 s. (**b**) Time at 0.2 s, 0.25 s, and 0.3 s.

In Figure 7, T_{min} is the overall lowest temperature, T_{max} is the highest temperature overall, T_{cmin} is the lowest temperature of the isotherm, and T_{cmax} is the highest temperature of the isotherm. The red words in the Figure 7a are the explanation of the contour in the corresponding position. It can be seen from Figure 7 that the temperature field of the upper surface of the substrate is mainly affected by two parts: the metal melt flowing out of the coating head and the arc heat source. The blank part of the molten pool is caused by the concave surface of the molten pool caused by the arc pressure.

In order to obtain the solidification rate, the solid phase fraction of the molten pool cross-section at different times was calculated as shown in Figure 8, where blue represents the solid phase, red represents the liquid phase, and between the two colors is the mushy region.

The surface of the molten pool in Figures 6d and 8c is significantly higher than that of the substrate due to the continuous forward movement of the welding arc. During the peak current period, the molten pool is concave under the action of the arc forces, and the fluid in the molten pool is pushed to the rear. The variation curve of d_H and d_V with time from the highest temperature point to solidification in the molten pool obtained through software postprocessing is shown in Figure 9. The cooling curve of T_p point is shown in Figure 10.

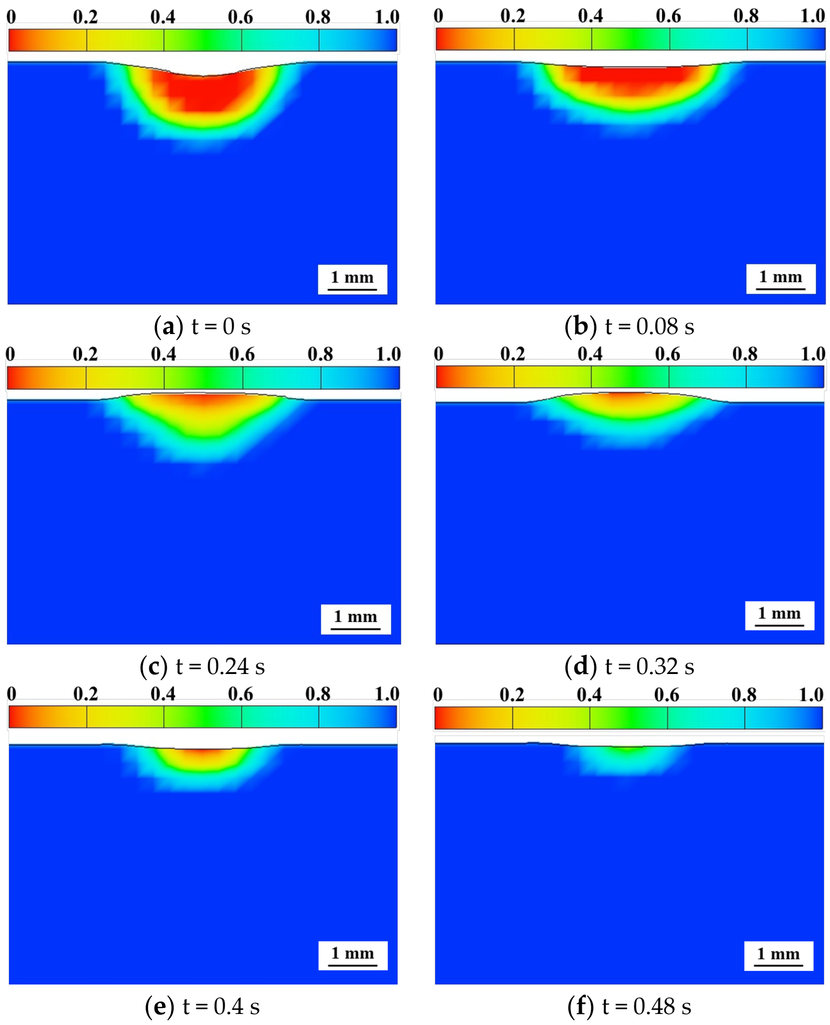

Figure 8. Solid phase fraction of molten pool cross-section at different times.

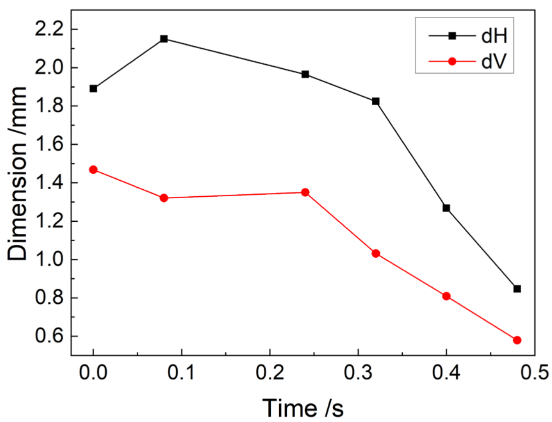

Figure 9. The variation curve of d_H and d_V with time.

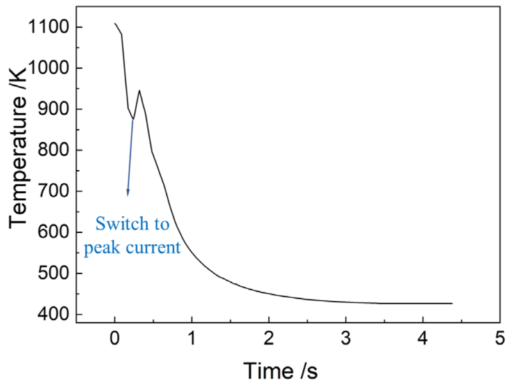

Figure 10. The cooling curve of T_p point.

The sudden increase in temperature at the molten pool center in Figure 10 is caused by the switching of the welding current from the base current to the peak current. According to Figures 9 and 10, the values of G/R and G·R at the fusion line of the molten pool at different times in the horizontal and vertical directions were calculated, and the results are shown in Figure 11.

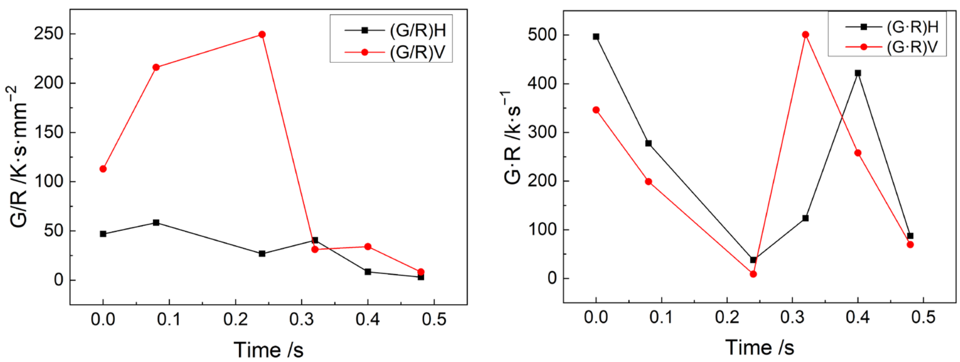

(**a**) G/R (**b**) G·R

Figure 11. The values of G/R and G·R at different times of the molten pool.

Since the values of d_H, d_V, and T_p were not monotonic over time, the values of G and R fluctuated all the time. As a result, the G/R and G·R values in Figure 11 were not monotonic, either. Using the same calculation method, the values of G/R and G·R during the solidification process of a single fused-coating layer can be obtained. The time when the coating layer begins to solidify is set to be the initial moment, and the result is shown in Figure 12.

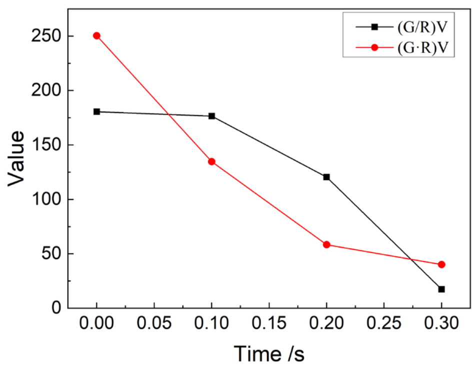

Figure 12. The values of G/R and G·R during the solidification process of fused coating.

4. Discussion

4.1. Analysis of Microstructure Morphology of Preheating Molten Pool and Coating Layer

As shown in Figure 12, the values of G/R and G·R during the solidification of the coating layer fluctuate less than those during the solidification of the molten pool. This is mainly because the coating layer gradually moves away from the arc during the solidification process and is less affected by changes in pulse current. The relationship between microstructure morphology, solidification rate, and temperature gradient is shown in Figure 13 [32].

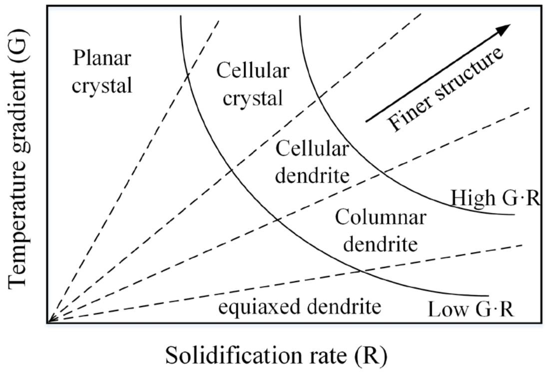

Figure 13. Relationship between microstructure morphology, solidification rate, and temperature gradient.

Temperature gradient and solidification rate play an important role in the microstructure morphology of the aluminum alloy after solidification. Usually, the G/R controls the solidification mode, while G·R governs the scale of solidified microstructure. As shown in Figure 11, when the solidification rate is low and the temperature gradient is high, it tends to generate planar crystals during the solidification process. When the curing rate increases and the temperature gradient remains high, there is a tendency to form cell crystals that regenerate into dendrites during the curing process. When the temperature gradient is low, columnar or equiaxed crystals will be generated during the solidification process. In short, an increase in the G·R value represents an increase in cooling rate and a gradually finer microstructure.

According to solidification theory, the microstructure of fused coating is mainly formed through grain nucleation and growth during the solidification stage of the melt pool. During the solidification process of metal alloys, the redistribution of solute causes a change in solute concentration at the solidification front, resulting in a difference between the actual and theoretical solidification temperature. The difference is also known as undercooling. According to the component undercooling theory, the existence of component undercooling is a necessity and sufficient for the instability of the solidification interface. Therefore, whether the components at the solidification front are subcooled is a criterion for determining whether the solid−liquid interface is in a stable state. The stability of the solidification front can be determined according to the G/R value. The criterion for judging the undercooling at the solidification front is shown in Equation (5):

$$G/R < \Delta T_E/D_L \tag{5}$$

where ΔT_E is the equilibrium solidification temperature range under a given component and D_L is the solute diffusion coefficient. For 2024 aluminum alloy, the values of ΔT_E and D_L are 94 K and 2.8×10^{-3} mm^2/s respectively, so $\Delta T_E/D_L = 3.36 \times 10^4$ Ks/ mm^2, which is much higher than the value of G/R; therefore, the solidification front is in an unstable state.

As heat is extracted from the substrate, solidification proceeds directionally from the substrate to the molten liquid. During solidification, solute atoms are repelled into the melt and a solute accumulation layer is formed before the solid−liquid interface. The grains in the columnar crystal region are arranged perpendicular to the wall and parallel to the direction of heat flow, exhibiting anisotropy. The grains in equiaxed crystals have small differences in size in each direction. According to the theory of constitutional supercooling, as the solidified layer moves inward, the heat dissipation capacity of the solid phase gradually weakens, the internal temperature gradient tends to be flat, and the solute atoms in the liquid phase become more and more enriched, so that the component supercooling in front of the interface gradually increases. It is generally accepted that the transport of heat and solute during solidification has great significance in determining the final grain size and morphology. The steep temperature gradient and rapid solidification rate result in columnar grain growth from the molten pool boundary [3]. When the constitutional supercooling is large enough to cause heterogeneous nucleation, it leads to the formation of internal equiaxed crystals. When the value of G/R decreases, the microstructure of the solidification interface gradually changes from columnar crystals to columnar dendrites and equiaxial crystals. Therefore, it can be concluded that the microstructure near the fusion line at the bottom of the molten pool after solidification is columnar crystals, and the microstructure near the center of the molten pool is equiaxed crystals. It can also be inferred that the bottom of the single coating layer is columnar crystal, and the top is equiaxed crystal.

4.2. Experimental Verification

The preheated molten pool is cut along the cross-section using wire cutting after solidification. Then the molten pool area is ground using 800 mesh, 1000 mesh, and 1500 mesh sandpaper in sequence and corroded using Keller's reagent. The microstructure of the junction area between the bottom of the melt pool and the heat-affected zone (zone 1) and the upper area of the melt pool (zone 2) is shown in Figure 14.

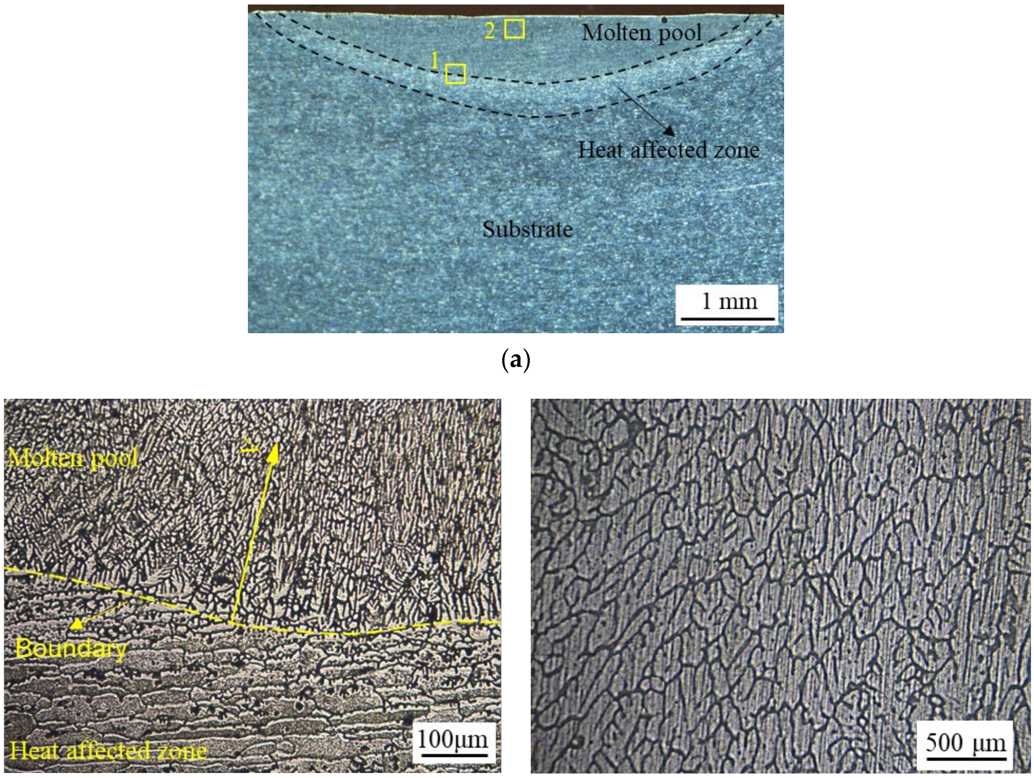

(**a**)

(**b**) (**c**)

Figure 14. Microstructural morphology of different areas inside the molten pool. (**a**) Observation position of preheated molten pool. (**b**) Microstructure morphology of zone 1. (**c**) Microstructure morphology of zone 2.

The microstructure inside the single coating layer was obtained by the same processing method. The observation position and the corresponding microstructure are shown in Figure 15.

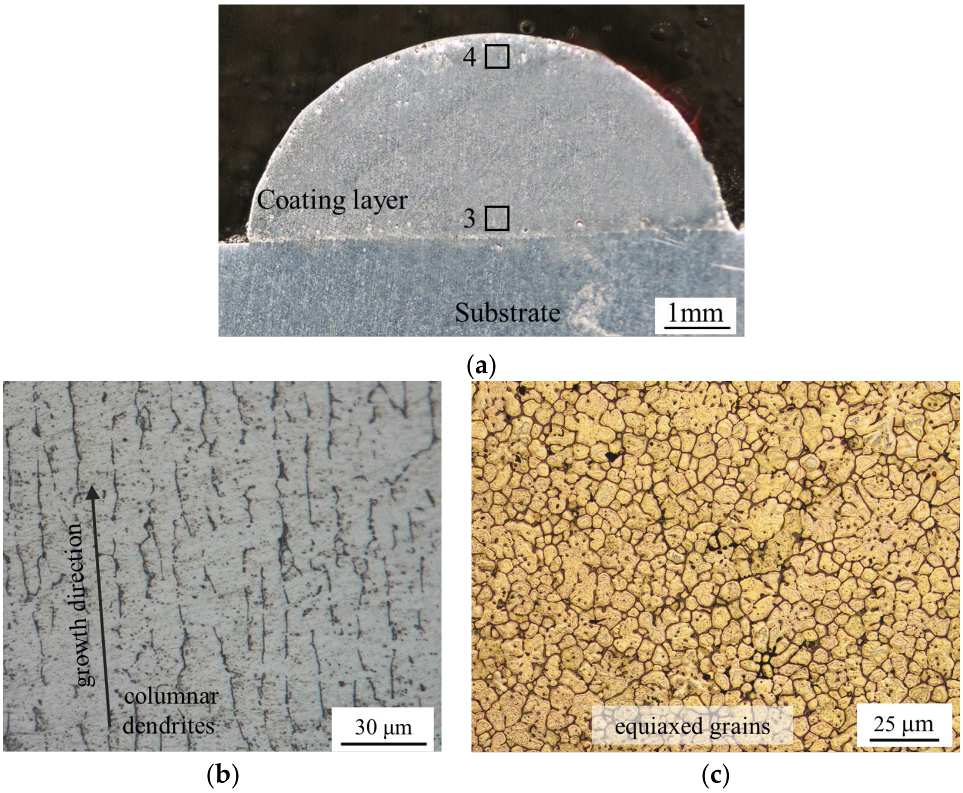

Figure 15. Microstructural morphology of different areas inside the coating layer. (**a**) Observation of the position of the microstructure of the coating layer. (**b**) Microstructure morphology of zone 3. (**c**) Microstructure morphology of zone 4.

The microstructure of the aluminum alloy after solidification in a molten pool mainly depends on the comprehensive effect of solute concentration, crystallization rate, and temperature gradient in the liquid phase. When the solute concentration and crystallization rate are constant, the temperature gradient in the crystallization region determines the morphology of the solidification structure. Once the high-temperature molten melt (973 K) in the crucible flows out of the nozzle and comes into contact with the cool substrate (298 K), solidification begins at the solid−liquid interface. Meanwhile, the top half of the melt has not yet begun to solidify because of a small temperature gradient. Many grains with different orientations near the solid−liquid interface at the bottom are in a semi-molten state. The liquid aluminum alloy can effectively wet the surface of these semi-molten grains, providing conditions for heterogeneous nucleation and crystallization. Then, the columnar dendrites begin to form at the bottom of the cladding layer. Due to the high thermal conductivity of aluminum alloys, there is a large temperature gradient near the fusion line of the molten pool. Although the crystallization area of 2024 aluminum alloy is relatively wide, it still crystallizes in a "layer by layer" manner. With the growth of columnar crystals and the precipitation of crystallization latent heat, the temperature gradient in the upper region of the molten pool becomes smaller, the remaining aluminum alloy in the molten pool begins to crystallize in a "mushy crystal" manner, and the crystalline morphology begins to evolve into equiaxed crystals. As the crystallization progresses, the equiaxed grains grow in a random direction in front of the columnar region. As a result, the equiaxed grains suppress the growth of the columnar front. Therefore, from Figures 14 and 15, it can be seen that the grains in the heat-affected zone are the coarsest, which are planar crystals.

The microstructure at the bottom of the molten pool and the coating layer grew in the form of columnar crystals, and began to change into equiaxed crystals at the top of the molten pool and the coating layer, which is consistent with the calculated results.

5. Conclusions

A comprehensive three-dimensional heat transfer and fluid flow model was used to simulate the heat flow field, molten pool size, the geometry of the fusion zone, and solidification parameters during the 2024 aluminum alloy coating forming process. Based on the theory of constitutional supercooling, the microstructure morphology of the pre-heated molten pool and deposition layer was inferred and experimentally verified. The qualitative prediction of microstructure morphology through solidification parameters is feasible. Compared with the simulation method of dendrite growth, this approach is simpler and applicable to other forming technologies involving metal solidification. The main conclusions drawn from the investigation are as follows:

1. The temperature gradient on the substrate surface is jointly affected by the melt flowing out of the nozzle and the arc, and the surface of the melt pool fluctuates up and down under the action of arc forces.
2. Temperature gradient and solidification rate play an important role in the microstructure morphology of the aluminum alloy after solidification. Since the temperature of the aluminum alloy melt in the crucible is only slightly higher than the complete melting temperature, and the arc is only used to form a shallow melt pool to enhance interlayer bonding force, the values of $G \cdot R$ and G/R are much smaller than those of mainstream additive manufacturing technologies. The cooling rate reached 250.5 K/s during Al fused coating. The welding machine current switches between the base and peak values, resulting in fluctuations in the values of G and R. An increase in $G \cdot R$ value represents an increase in cooling rate and a gradually finer microstructure.
3. The solidification front is in an unstable state during the 2024 aluminum alloy fused-coating process. The microstructure at the bottom of the molten pool and coating layer is columnar crystal, while the microstructure at the upper part is equiaxed crystal.

Author Contributions: Conceptualization, G.Z. and X.Y.; methodology, G.Z.; software, G.Z.; validation, G.Z. and J.Z.; investigation, G.Z. and J.Z.; resources, G.Z.; writing—original draft preparation, G.Z.; visualization, J.Z.; supervision, X.Y.; funding acquisition, X.Y. All authors have read and agreed to the published version of the manuscript.

Funding: This research was funded by the National Natural Science Foundation of China, grant number 52075306.

Data Availability Statement: Not applicable.

Acknowledgments: The authors thank Shandong Provincial Key Laboratory of Precision Manufacturing and Non-traditional Machining for providing metallographic observation equipment.

Conflicts of Interest: The authors declare no conflict of interest.

References

1. Xi, K.; Wu, H.; Zhou, C.; Qi, Z.; Yang, K.; Fu, R.; Xiao, S.; Wu, G.; Ding, K.; Chen, G.; et al. Improved corrosion and wear resistance of micro-arc oxidation coatings on the 2024 aluminum alloy by incorporation of quasi-two-dimensional sericite microplates. *Appl. Surf. Sci.* **2022**, *585*, 152693. [CrossRef]
2. Armstrong, M.; Mehrabi, H.; Naveed, N. An overview of modern metal additive manufacturing technology. *J. Manuf. Process.* **2022**, *84*, 1001–1029. [CrossRef]
3. Liu, Z.; Zhao, D.; Wang, P.; Yan, M.; Yang, C.; Chen, Z.; Lu, J.; Lu, Z. Additive manufacturing of metals: Microstructure evolution and multistage control. *J. Mater. Sci. Technol.* **2022**, *100*, 224–236. [CrossRef]
4. Kim, I.; Kim, M.; Kim, H.; Lee, M.; Jeon, Y. Laser Cladding of Al 102 Powder on Al 4047 with Direct Energy Deposition. *Metals* **2023**, *13*, 856. [CrossRef]

5. Pu, Z.; Du, D.; Wang, K.; Liu, G.; Zhang, D.; Zhang, H.; Xi, R.; Wang, X.; Chang, B. Study on the NiTi shape memory alloys in-situ synthesized by dual-wire-feed electron beam additive manufacturing. *Addit. Manuf.* **2022**, *56*, 102886. [CrossRef]
6. Omiyale, B.; Olugbade, T.; Abioye, T.; Farayibi, P. Wire arc additive manufacturing of aluminium alloys for aerospace and automotive applications: A review. *Mater. Sci. Technol.* **2022**, *38*, 391–408. [CrossRef]
7. Gu, D.; Rao, X.; Dai, D.; Ma, C.; Xi, L.; Lin, K. Laser additive manufacturing of carbon nanotubes (CNTs) reinforced aluminum matrix nanocomposites: Processing optimization, microstructure evolution and mechanical properties. *Addit. Manuf.* **2019**, *29*, 100801. [CrossRef]
8. Wang, Q.; Lin, X.; Kang, N.; Wen, X.; Cao, Y.; Lu, J.; Peng, D.; Bai, J.; Zhou, Y.; Mansori, M.; et al. Effect of laser additive manufacturing on the microstructure and mechanical properties of TiB_2 reinforced Al-Cu matrix composite. *Mater. Sci. Eng. A* **2022**, *840*, 142950. [CrossRef]
9. Fu, R.; Tang, S.; Lu, J.; Cui, Y.; Li, Z.; Zhang, H.; Xu, T.; Chen, Z.; Liu, C. Hot-wire arc additive manufacturing of aluminum alloy with reduced porosity and high deposition rate. *Mater. Des.* **2021**, *199*, 109370. [CrossRef]
10. Ye, Z.; Su, M.; Li, J.; Jing, C.; Xu, S.; Liu, L.; Ren, G.; Wang, X. Laser nano-technology of light materials: Precision and opportunity. *Opt. Laser Technol.* **2021**, *139*, 106988. [CrossRef]
11. Fiedor, P.; Ortyl, J. A new approach to micromachining: High-precision and innovative additive manufacturing solutions based on photopolymerization technology. *Materials* **2020**, *13*, 2951. [CrossRef]
12. Guzzi, E.; Tibbitt, M. Additive manufacturing of precision biomaterials. *Adv. Mater.* **2020**, *32*, 1901994. [CrossRef] [PubMed]
13. Monteiro, H.; Carmona-Aparicio, G.; Lei, I.; Despeisse, M. Energy and material efficiency strategies enabled by metal additive manufacturing–A review for the aeronautic and aerospace sectors. *Energy Rep.* **2022**, *8*, 298–305. [CrossRef]
14. Shahwaz, M.; Nath, P.; Sen, I. A critical review on the microstructure and mechanical properties correlation of additively manufactured nickel-based superalloys. *J. Alloys Compd.* **2022**, *907*, 164530. [CrossRef]
15. Narasimharaju, S.; Zeng, W.; See, T.; Zhu, Z.; Scott, P.; Jiang, X.; Lou, S. A comprehensive review on laser powder bed fusion of steels: Processing, microstructure, defects and control methods, mechanical properties, current challenges and future trends. *J. Manuf. Process.* **2022**, *75*, 375–414. [CrossRef]
16. Zhang, Z.; Wang, Y.; Ge, P.; Wu, T. A review on modelling and simulation of laser additive manufacturing: Heat transfer, microstructure evolutions and mechanical properties. *Coatings* **2022**, *12*, 1277. [CrossRef]
17. Tourret, D.; Liu, H.; Llorca, J. Phase-field modeling of microstructure evolution: Recent applications, perspectives and challenges. *Prog. Mater. Sci.* **2022**, *123*, 100810. [CrossRef]
18. Ghumman, U.; Fang, L.; Wagner, G.; Chen, W. Calibration of Cellular Automaton Model for Microstructure Prediction in Additive Manufacturing Using Dissimilarity Score. *J. Manuf. Sci. Eng.* **2023**, *145*, 061002. [CrossRef]
19. Chao, X.; Qi, L.; Ma, W.; Ge, J.; Tian, W. Monte carlo based strategy to simulate the microstructure evolution of the short-fiber reinforced metal matrix composites. *Mater. Today Commun.* **2022**, *33*, 104275. [CrossRef]
20. Hosseinzadeh, H.; Nematollahi, M.; Safaei, K.; Abedi, H.; Bayati, P.; Javan, R.; Poorganji, B.; Yuan, L.; Elahinia, M. A numerical approach to model microstructure evolution for NiTi shape memory alloy in laser powder bed fusion additive manufacturing. *Integrating Mater. Manuf. Innov.* **2022**, *11*, 121–138. [CrossRef]
21. Panchenko, O.; Kladov, I.; Kurushkin, D.; Zhabrev, L.; Ryl'kov, E.; Zamozdra, M. Effect of thermal history on microstructure evolution and mechanical properties in wire arc additive manufacturing of HSLA steel functionally graded components. *Mater. Sci. Eng. A* **2022**, *851*, 143569. [CrossRef]
22. Yan, X.; Yang, X.; Tian, G.; Sun, D.; Liu, S.; Xiong, Z.; Wen, Z.; Xu, Q. Modeling and Simulation Investigations on Microstructure Evolution during Additive Manufacturing of AlSi10Mg Alloy. *Metals* **2022**, *12*, 1711. [CrossRef]
23. Xue, T.; Gan, Z.; Liao, S.; Cao, J. Physics-embedded graph network for accelerating phase-field simulation of microstructure evolution in additive manufacturing. *NPJ Comput. Mater.* **2022**, *8*, 201. [CrossRef]
24. Du, J.; Wei, Z. Numerical investigation of thermocapillary-induced deposited shape in fused-coating additive manufacturing process of aluminum alloy. *J. Phys. Commun.* **2018**, *2*, 115013. [CrossRef]
25. Fang, X.; Du, J.; Wei, Z.; He, P.; Bai, H.; Wang, X.; Lu, B. An investigation on effects of process parameters in fused-coating based metal additive manufacturing. *J. Manuf. Process.* **2017**, *28*, 383–389. [CrossRef]
26. Wang, X.; Xiao, H.; Li, H.; Liu, F.; Zuqiang, S.; Tan, F. Detection and control of the morphology of TIG-metal fused coating additive manufacturing. *J. Mech. Sci. Technol.* **2021**, *35*, 2161–2166.
27. Zhao, G.; Du, J.; Wei, Z.; Xu, S.; Geng, R. Numerical analysis of aluminum alloy fused coating process. *J. Braz. Soc. Mech. Sci. Eng.* **2020**, *42*, 1–9. [CrossRef]
28. Du, J.; Wei, Z.; Zhang, Y.; Zhou, S. Numerical simulation and experimental research on fused-coating additive manufacturing of Sn63Pb37 thin-walled structures. *Appl. Phys. A* **2019**, *125*, 1–10. [CrossRef]
29. Sigworth, G. Fundamentals of solidification in aluminum castings. *Int. J. Met.* **2014**, *8*, 7–20. [CrossRef]
30. An, Y.; Liang, L.; Xu, X.; Zhao, Y.; Hou, H. Effect of bulk undercooling on microstructure transformation mechanism of rapidly solidified nickel alloys. *J. Mater. Res. Technol.* **2021**, *11*, 548–563. [CrossRef]

31. Farzadi, A.; Serajzadeh, S.; Kokabi, A. Modeling of heat transfer and fluid flow during gas tungsten arc welding of commercial pure aluminum. *Int. J. Adv. Manuf. Technol.* **2008**, *38*, 258–267. [CrossRef]
32. Kou, S. *Welding Metallurgy*, 2nd ed.; John Wiley &Sons, Inc.: Hoboken, NJ, USA, 2003; pp. 223–225.